Ultra-precision grinding process and compensation of cylindrical structure array mold

Journal Pre-proofs

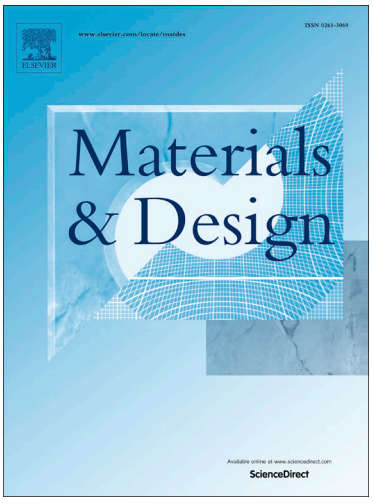

Ultra-precision grinding process and compensation of cylindrical structure array mold

Peng Gu, Kaixuan Zhou, Zhiyuan Li, Andrea Mura, Rumeng Yang, Pengfei Zhang, Yingchen Sun, Chuanmin Zhu

PII: S0264-1275(26)00967-6
DOI: https://doi.org/10.1016/j.matdes.2026.116394
Reference: JMADE 116394

To appear in: *Materials & Design*

Received Date: 9 February 2026
Revised Date: 21 May 2026
Accepted Date: 10 June 2026

Please cite this article as: Gu, P., Zhou, K., Li, Z., Mura, A., Yang, R., Zhang, P., Sun, Y., Zhu, C., Ultra-precision grinding process and compensation of cylindrical structure array mold, *Materials & Design* (2026), doi: https://doi.org/10.1016/j.matdes.2026.116394

Declaration of interests

☒ The authors declare that they have no known competing financial interests or personal relationships that could have appeared to influence the work reported in this paper.

☐ The authors declare the following financial interests/personal relationships which may be considered as potential competing interests:

Graphic Abstract

WC-Co carbide cylindrical array molds are essential for the high-efficiency manufacturing of high-precision optical lenses. However, due to the extreme hardness, brittleness, and complex dynamic mechanical response of the material, achieving high-efficiency and high-precision machining while suppressing surface damage remains a critical challenge. By utilizing a calibrated JH-2 constitutive model, this work analyzes the material removal mechanisms of WC-Co to disclose dynamic failure behaviors and define the critical depth threshold for ductile-regime removal. Subsequently, a hybrid grinding strategy is developed by integrating rough grinding via a profile diamond wheel with fine compensation using an ultra-thin diamond wheel, complemented by a constant material removal rate global path planning method. Experimental results demonstrate that the proposed approach achieves a form accuracy (PV) of 2.43 μm and a surface roughness (Sa) of 17.025 nm for the array mold, with excellent morphological uniformity.

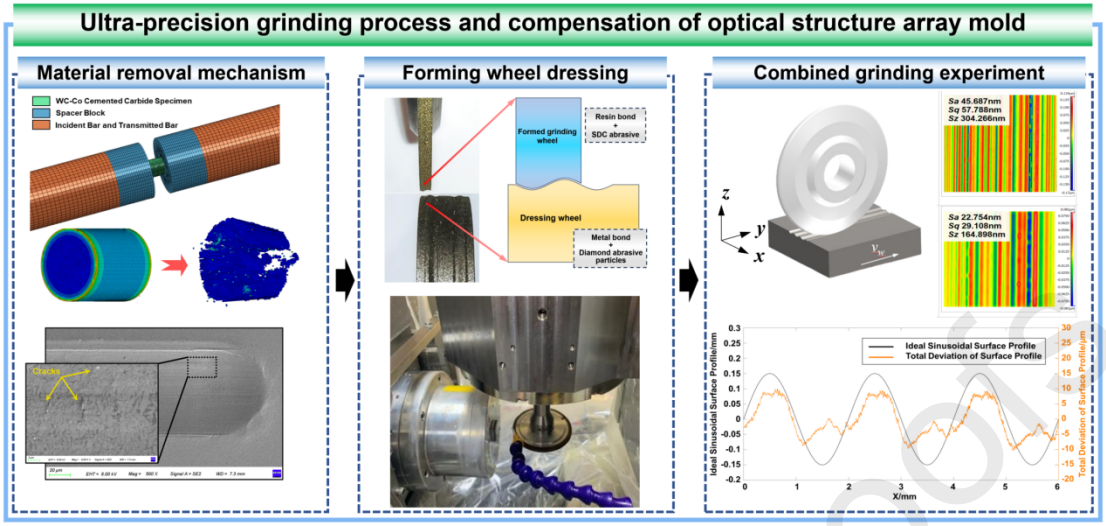

Research Highlights

- A microscopic simulation model of WC-Co cemented carbide was established.
- A hybrid grinding process using profiled grinding wheels and ultra-thin grinding wheels was proposed.
- An ultra-thin wheel trajectory planning strategy optimized for cylindrical arrays was proposed and verified.

Ultra-precision grinding process and compensation of cylindrical structure array mold

Peng Gu[a] Kaixuan Zhou[a] Zhiyuan Li[b] Andrea Mura[c] Rumeng Yang[b]

Pengfei Zhang[b] Yingchen Sun[b] Chuanmin Zhu[b*]

a College of Mechanical Engineering, Donghua University, Shanghai 201620, China

b School of Mechanical Engineering, Tongji University, Shanghai 201804, China

c Department of Mechanical and Aerospace Engineering, Politecnico di Torino, Torino 10129, Italy

✉ 01065@tongji.edu.cn

Abstract: WC-Co carbide cylindrical array molds are essential for the high-efficiency manufacturing of high-precision optical lenses. However, due to the extreme hardness, brittleness, and complex dynamic mechanical response of the material, achieving high-efficiency and high-precision machining while suppressing surface damage remains a critical challenge. By utilizing a calibrated JH-2 constitutive model, this work analyzes the material removal mechanisms of WC-Co to disclose dynamic failure behaviors and define the critical depth threshold for ductile-regime removal. Subsequently, a hybrid grinding strategy is developed by integrating rough grinding via a profile diamond wheel with fine compensation using an ultra-thin diamond wheel, complemented by a constant material removal rate global path planning method. Experimental results demonstrate that the proposed approach achieves a form accuracy PV of 2.43 μm and a surface roughness Sa of 17.025 nm for the array mold, with excellent morphological uniformity. These results indicate that the proposed strategy is beneficial not only for deterministic form generation, but also for suppressing brittle damage and preserving the surface integrity required for functional structured molds.

Keywords: WC-Co carbide; sinusoidal cylindrical array; ductile-regime removal; hybrid grinding; constant material removal rate

1 Introduction

Driven by the ongoing trend toward miniaturization and high integration in optical systems, the demand for high-precision microstructured array lenses has increased significantly [1]. Characterized by their lightweight architecture, compactness, and scalability for mass replication, as well as unique optical properties such as high diffraction efficiency and design flexibility, these arrays are extensively utilized in frontier domains including medical diagnostics, aerospace, national defense, astronomical observation, and modern optical communication systems [2-4]. As pivotal components in these systems, cylindrical array lenses play a decisive role, and their fabrication quality directly governs energy transmission stability and beam homogenization performance. Currently, precision glass molding represents the predominant strategy for the high-efficiency and cost-effective manufacturing of such components [5]. Consequently, WC-Co cemented carbide, owing to its exceptional hardness, wear resistance, and thermomechanical stability, has emerged as the critical substrate material for fabricating these ultra-precision molds [6-7].

Ultra-precision grinding is a key technology for achieving nanometer-level surface quality and sub-micron form accuracy on high-hardness molds [8-9]. However, for WC-Co cemented carbide, the grinding process is frequently accompanied by crack initiation, subsurface damage, and unstable material removal because of its high hardness, brittle fracture tendency, and multiphase heterogeneity. Existing studies have investigated the machining response of hard-brittle materials from the perspectives of grinding-induced damage, local contact deformation, and strain-rate-dependent constitutive behavior. Wu C et al. [10] examined the ground microstructure of silicon carbide after high-speed grinding and quantitatively related subsurface damage, fracture characteristics, and specific grinding energy to the ductile grinding mechanism. For WC-Co hardmetals, Duszová A et al. [11] employed instrumented indentation

to characterize the hardness and indentation modulus of the WC and Co phases, revealing the influence of microstructural features on local mechanical response. Liu Y et al. [12] further showed through nanoindentation/scratch tests that the brittle-to-plastic transition is strongly affected by loading condition and interface response, indicating that the local removal mode is highly sensitive to penetration depth and stress state. Beyond indentation- and scratch-based analyses, recent studies have emphasized that the material response during abrasive interaction cannot be fully understood without considering dynamic loading effects. Gao Y et al. [13] established a dynamic constitutive relation for fine-grained WC-Co composites and clarified their failure behavior under dynamic compression. Jia X et al. [14] reported comparable strain-rate-sensitive compressive failure characteristics in hard-brittle ceramics, suggesting that transient stress evolution plays a decisive role in crack initiation and fragmentation. Zhao L et al. [15] also combined finite element simulation with nanoindentation experiments to reveal the interplay between ductile-brittle deformation and crack evolution in 3C-SiC under Berkovich indentation. Although these studies provide an important basis for understanding deformation and damage evolution in hard-brittle materials, the high-strain-rate removal behavior of WC-Co cemented carbide under ultra-precision grinding conditions remains insufficiently clarified. In particular, the critical threshold governing the transition from ductile-regime removal to brittle fracture has not yet been clearly identified. Therefore, it is necessary to establish a stable ductile-regime machining window for the rational design of grinding parameters and subsequent compensation strategies.

To achieve high-efficiency manufacturing within the identified deterministic machining windows, an appropriate grinding strategy is required for surface generation [16]. Existing studies have shown that ordered abrasive distributions and profile-controlled grinding tools can improve grinding efficiency and surface integrity by stabilizing the local wheel–workpiece interaction. Butler S et al. [17] reported that, compared with conventional grinding tools, precisely controlled abrasive arrays distribute the grinding load more uniformly, thereby enabling more efficient material removal while significantly improving ground surface quality and tool service life. Zhang J et al. [18] further demonstrated that monolayer brazed ordered diamond wheels, when accurately dressed, can realize ductile-regime grinding of zirconia ceramics and markedly reduce grinding surface roughness. Likewise, Wu Q et al. [19] showed that diamond fiber ordered-arrangement wheels produce better surface integrity, with fewer macro-cracks and lower roughness than ordinary dressed wheels. These studies indicate that profile-controlled or ordered grinding wheels are advantageous for bulk material removal and overall form generation. However, for cylindrical array molds with stringent form-accuracy requirements, high-efficiency profile generation alone is insufficient. In this respect, ultra-thin grinding wheels offer a different capability. Chen S et al. [20] developed an ultra-thin diamond grinding wheel for machining micro-grooves on optical glass, in which a wheel with a grain size of 0–2 μm was fabricated by micro-co-deposition and then reduced by wire-EDM, demonstrating the feasibility of ultra-thin wheels for high-resolution microstructured fabrication. Nevertheless, when such tools are used alone for full-scale material removal, the process becomes inefficient and more sensitive to wheel wear, local contact variation, and trajectory organization. Pimenov D et al. [21] pointed out that the continuous alteration of wheel geometry and contact conditions leads to inconsistent material removal, which

significantly compromises dimensional accuracy and surface integrity. This issue becomes even more pronounced in cylindrical arrays, where not only the profile accuracy of a single unit but also the dimensional consistency among repeated units must be controlled simultaneously. Under these conditions, path planning is no longer a secondary issue, but a key factor governing removal uniformity and machining efficiency. Guo P et al. [22] proposed a feature-adaptive toolpath planning strategy based on equal chord length and equal cutting residual area, which improved the surface texture parameters of LED lenses by 17.51% and 57.64%, respectively. Liu J et al. [23] likewise showed that a free-curve-based path planning method could reduce processing time by 25% and decrease the surface roughness Ra from 0.6 μm to 0.4 μm. Beyond trajectory design, high-precision fabrication of optical structure arrays also requires compensation to be integrated into the machining chain. Wu C et al. [24] proposed an accelerated point-cloud registration methodology for optical freeform surfaces, reducing the PV error by 3.95 times. Yu S et al. [25] developed a compensation method for aspheric cylindrical lens arrays based on the real-time wheel contour and normal residual, decreasing the shape error by 91%, while Xu L et al. [26] further reduced the wheel arc contour error from 0.031 mm to 0.019 mm through machine-vision-based contour measurement and dressing-error compensation. Therefore, for cylindrical array molds with complex geometry, neither profile grinding alone nor ultra-thin-wheel machining alone can simultaneously satisfy the requirements of removal efficiency, deterministic form generation, and localized precision correction. A hybrid grinding strategy that combines high-efficiency profile generation with subsequent ultra-thin-wheel compensation is therefore necessary to ensure material-removal consistency, coordinated path planning, and high form accuracy.

Despite the progress outlined above, a systematic framework for the high-efficiency and high-precision grinding of sinusoidal cylindrical array molds has not yet been established. To address this gap, this study investigates ultra-precision grinding and form compensation of cylindrical array molds. First, the fundamental mechanical behavior of WC-Co cemented carbide is characterized under quasi-static and dynamic loading, and a calibrated JH-2 constitutive model is established to describe its high-strain-rate response during ultra-precision grinding. Second, the material-removal and deformation behavior of WC-Co is studied through scratch experiments and simulations, from which the approximate brittle-to-ductile transition condition is inferred and a ductile-regime grinding-depth range for subsequent process development is established. Finally, a hybrid grinding strategy is proposed by combining high-efficiency profile generation with deterministic ultra-thin-wheel compensation, together with a global path-planning method incorporating equal residual height and constant material removal rate. The effectiveness of the proposed strategy in improving machining accuracy and efficiency, while suppressing brittle damage and preserving the surface integrity of WC-Co structured molds, is validated experimentally.

2 Material property experiment

2.1 Material property

WC-Co cemented carbide, a composite material synthesized via high-temperature sintering of tungsten carbide (WC) and cobalt (Co) powders, represents a typical metal-ceramic system produced through powder metallurgy. Owing to its exceptional combination of high hardness, wear resistance, flexural strength, and thermomechanical stability, this substrate has been extensively utilized in the mold fabrication industry. In this investigation, M78 cemented carbide was selected as the experimental specimen, with its fundamental mechanical properties and constituent parameters systematically summarized in Table 1. According to the material specifications, the specimen exhibits a nominal density of 14.2 g/cm³, with a chemical composition comprising 88.5% WC and 10.5% Co, supplemented by trace elements such as Ni to further refine its microstructural performance.

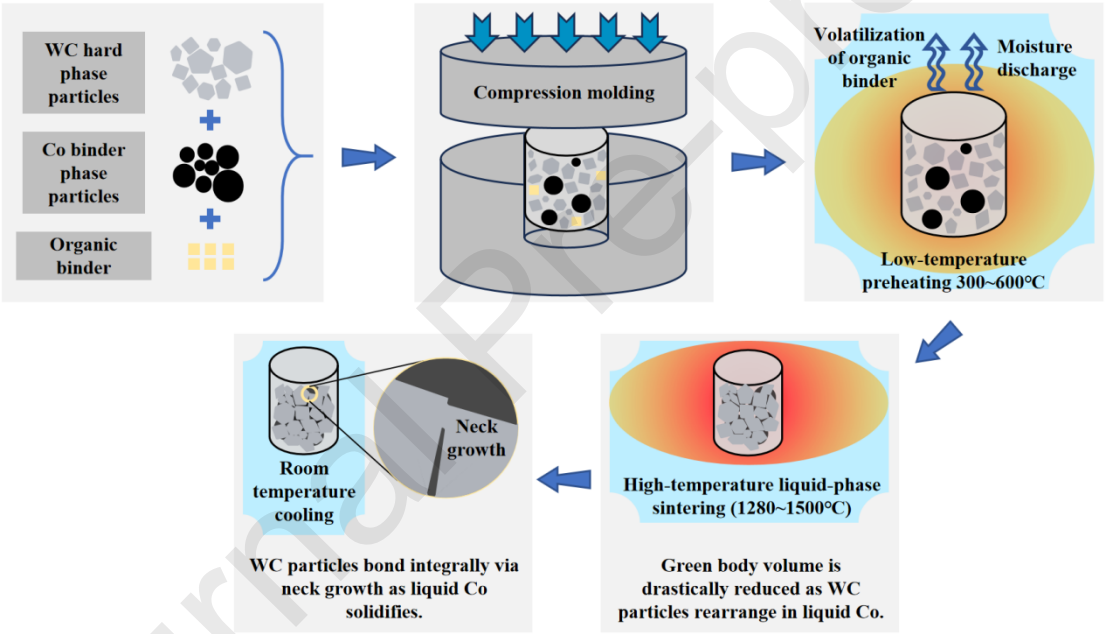

Figure 1 WC-Co cemented carbide preparation process

Table 1 Elemental composition table of WC-Co cemented carbide

Element	W	C	Co	Ni	Others
Content(%)	83.0	5.5	10.5	0.5	0.5

2.2 Material performance experiment

2.2.1 Experimental apparatus

The setup for the quasi-static compression test is an electronic universal testing machine. The WC-Co cemented carbide specimens were wire-cut from plate-shaped WC-Co cemented carbide M78 material, with a cylindrical shape of Φ5 mm × 5 mm. The physical diagrams of the test setup and specimens are shown in Figure 2(a-b). The SHPB setup for the dynamic mechanical properties test of WC-Co cemented carbide is shown in Figure 2(c). The specimen dimensions are consistent with those of the quasi-static compression test, the size of cylindrical specimens is Φ5 mm × 5 mm. Cemented carbide was used as spacers in the test, with the spacers having a diameter of 16 mm and a thickness of 10 mm. The end faces of the specimens and spacers were polished with sandpaper to ensure good parallelism, and molybdenum disulfide was used as a lubricant to reduce friction at each contact interface.

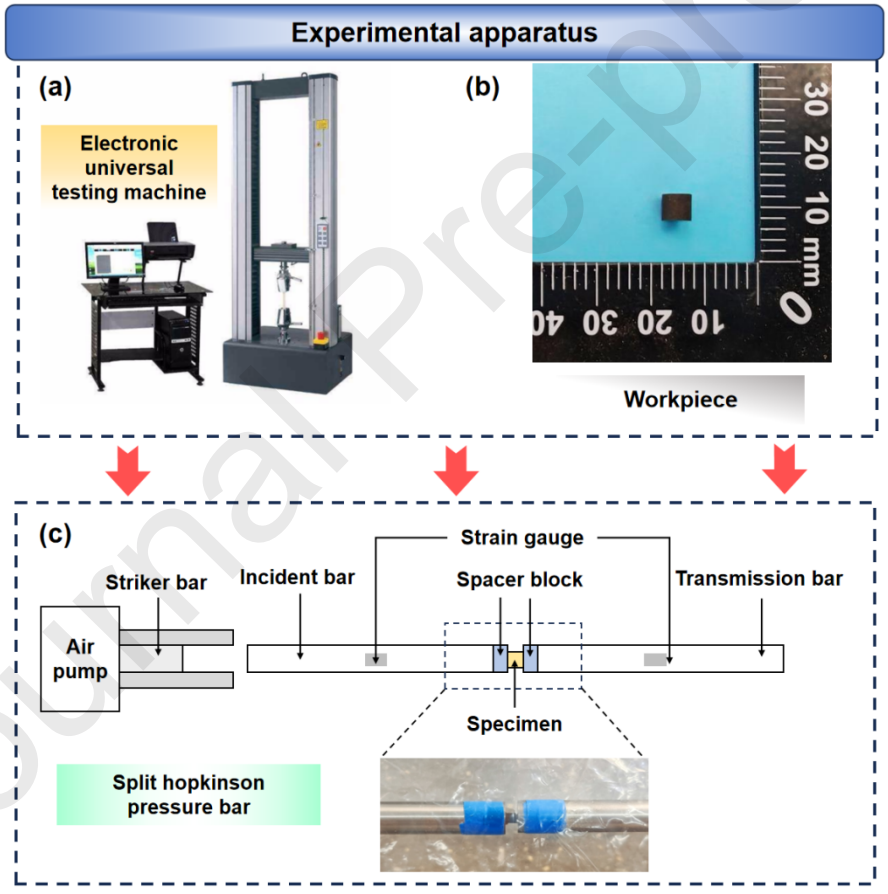

Figure 2 Physical diagrams of test facilities ((a) Electronic universal testing machine (b) WC-Co cemented carbide (c) SHPB setup)

2.2.2 Experimental process

Quasi-static compression tests were conducted at a low loading rate to characterize the constitutive behavior and fundamental mechanical properties of the substrate. WC-Co cemented carbide specimens with dimensions of Φ5 mm × 5 mm were fabricated by WEDM and used in the quasi-static compression tests. Prior to the WEDM process, the material surface was meticulously polished to a roughness of R_a 0.8 μm, with subsequent removal of surface burrs to minimize stress concentration effects. Figure 3(a) illustrates the typical stress-strain response at a strain rate of 0.001 s^{-1}. The curve exhibits a predominantly linear-elastic behavior, with a negligible degree of plastic deformation. Upon reaching the critical stress threshold, the specimen undergoes instantaneous fracture and catastrophic failure, a phenomenon that underscores the intrinsic brittleness of WC-Co cemented carbide. The quantitative mechanical indicators derived from three replicate tests are systematically summarized in Table 2.

Table 2 Results of quasi-static compression tests

Sequence number	$\dot{\varepsilon}$	σ/GPa	p/GPa	σ*/GPa	p*/GPa
1	0.001	4.40	6.3220	0.3387	0.8993
2	0.001	4.43	6.3601	0.3410	0.9047
3	0.001	4.45	6.3847	0.3426	0.9082

During the SHPB experiments, the high-strain-rate pulses, comprising incident, reflected, and transmitted waves, were recorded via high-sensitivity strain gauges mounted on the incident and transmission bars. Based on the one-dimensional stress wave propagation theory, the time-resolved variations of dynamic stress, strain rate, and strain were derived to establish the dynamic constitutive relationship of the substrate. Quantitatively, an impact pressure of 0.5 MPa corresponded to a strain rate of 230 s^{-1}, while impact pressures of 0.6 MPa and 0.7 MPa yielded strain rates of 396 s^{-1} and 510 s^{-1}, respectively. Stable wave signals with high reliability were obtained for all three loading conditions. Figure 3(b) illustrates the voltage-time profiles of the WC-Co specimens under dynamic loading conditions. It is observed that the stress wave propagates through the incident bar into the specimen and undergoes reflection at the loading interface. A pronounced signal plateau is visible in the reflected wave, followed by an abrupt decay to zero immediately after the peak. This characteristic wave profile signifies the instantaneous fracture and catastrophic failure of the specimen upon wave transmission, further corroborating the intrinsic brittle nature of the WC-Co cemented carbide under high-strain-rate deformation. The mechanical indicators derived from the dynamic tests are systematically summarized in Table 3.

Table 3 Results of SHPB tests

Sequence number	&	σ /GPa	p/GPa	σ *	p*
1	230	4.72	7.8203	0.3634	1.1120
2	396	4.87	7.9631	0.3749	1.1327
3	510	5.08	8.1176	0.3911	1.1547

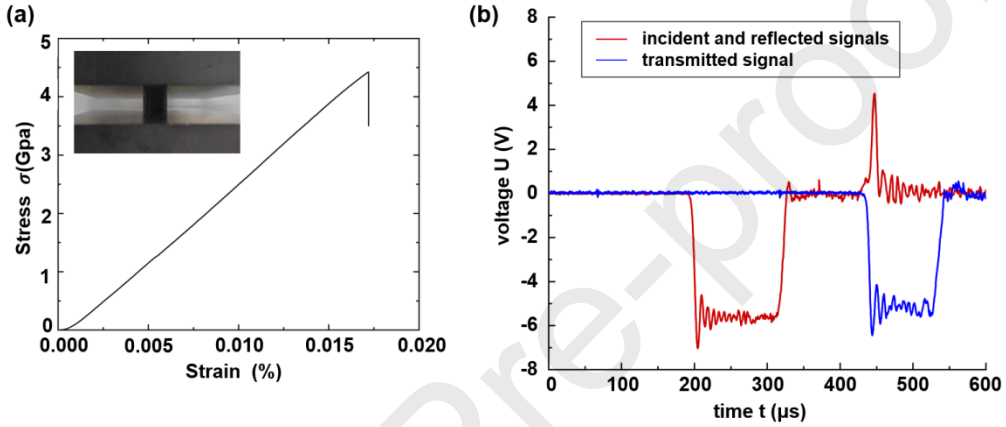

Figure 3 Quasi-static compression process and results((a) stress-strain curve at a strain rate of 0.001 s^{-1} (b) time-voltage curve of the SHPB test)

2.2.3 Experimental results

During experiments, rapid microcrack propagation and severe fragmentation of WC-Co specimens hindered capturing transient failure evolution, requiring a high-fidelity constitutive model for single-abrasive scratching simulations of material removal. The Johnson-Holmquist II (JH-2) model, robust for brittle materials and particle-reinforced composites under high-strain-rate impacts, fits this need well. WC-Co surfaces experience intense friction, stress concentration, and complex ductile-to-brittle transitions during scratching; the JH-2 model uniquely couples pressure-dependent strength with dynamic damage evolution to simulate transient stress responses, microcrack propagation, and material spalling in extreme conditions, so it is adopted to theoretically analyze deformation and removal behavior in dynamic scratch simulations.

The bulk modulus and shear modulus of the material can be calculated using Equations (1-2):

$$K_1 = \frac{E}{3(1-2\nu)} \quad (1)$$

$$G = \frac{E}{2(1+\nu)} \quad (2)$$

The parameters of the WC-Co cemented carbide used in this study are as follows: density of 14.2 g/cm³, Poisson's ratio of 0.215, and elastic modulus of 585.48 GPa. After calculation, the bulk modulus and shear modulus are obtained as K_1=342 GPa and G=241 GPa, respectively.

2.2.3.1 Equation of state

To characterize the high-pressure dynamic response of the substrate, Grady D et al. [27] conducted a series of plate impact experiments on WC-Co cemented carbide, establishing the correlation between shock wave velocities U_s and particle velocities U_p. By utilizing the least squares method for linear regression analysis, the Hugoniot relationship was derived as Us=5.376+0.821U_p. Based on the fundamental principles of shock wave physics and the Rankine-Hugoniot conservation relations, the volumetric strain μ and the resulting hydrostatic pressure p can be analytically defined through Equations (3-4):

$$\mu = \frac{\rho}{\rho_0} - 1 = \frac{U_p}{U_s - U_p} \quad (3)$$

$$p = \rho_0 U_s U_p \quad (4)$$

The least squares method was used to perform curve fitting on the calculated (p, μ) data. Since K_1 is known, the only fitting parameters are the material constants K_2 and K_3. The fitted equation of state for the p-μ relationship of WC-Co cemented carbide is:

$$p = K_1\mu + K_2\mu^2 + K_3\mu^3 = 342\mu + 1739\mu^2 - 7228\mu^3 \quad (5)$$

where K_2=1739 and K_3=-7228.

2.2.3.2 Undamaged strength model

In accordance with the three-dimensional Griffith yield criterion [28], the quasi-static compressive strength σ_s and Hugoniot elastic limit σ_{HEL} of brittle cemented carbide materials exhibit the following relationship:

$$\sigma_{HEL} = \frac{1-\nu^2}{(1-2\nu)^2}\sigma_s \quad (6)$$

Where σ_s is the quasi-static compressive strength. From the quasi-static compression test, the σ_s of WC-Co cemented carbide was obtained as 4.426 GPa, and the calculated Hugoniot elastic limit σ_{HEL} was 12.99 GPa. The Hugoniot elastic limit σ_{HEL} can be expressed in terms of the hydrostatic pressure tensor p_{HEL} and deviatoric stress tensor s_{HEL}, with the specific formula shown in Equation (7):

$$\sigma_{HEL} = p_{HEL} + \frac{2}{3} s_{HEL} \quad (7)$$

Hooke's Law establishes the intrinsic relationship between the distortion caused by the deviatoric stress tensor *s* and the volumetric strain μ, with its formula given in Equation (8):

$$s = 2G \frac{\mu}{\mu + 1} \quad (8)$$

After substitution, the relationship between σ_{HEL} and μ_{HEL} is obtained as shown in Equation (9):

$$\sigma_{HEL} = K_1 \mu_{HEL} + K_2 \mu_{HEL}^2 + K_3 \mu_{HEL}^3 + \frac{4}{3} G \frac{\mu_{HEL}}{1 + \mu_{HEL}} \quad (9)$$

The calculated results are: μ_{HEL} =0.01889 GPa， s_{HEL} =8.9362 GPa， p_{HEL} =7.0325 GPa. The relationship between strain rate and equivalent stress under different strain rates is shown in Equation (10):

$$\frac{\sigma_{i1}^*}{\sigma_{i2}^*} = \frac{A(P^* + T^*)^N [1 + C \ln(\dot{\varepsilon}_1)]}{A(P^* + T^*)^N [1 + C \ln(\dot{\varepsilon}_2)]} = \frac{1 + C \ln(\dot{\varepsilon}_1)}{1 + C \ln(\dot{\varepsilon}_2)} \quad (10)$$

By substituting the strain rates and yield strengths (under different strain rate conditions) from the SHPB test results into the above equation, the calculated value of *C* is 0.01043. The non-dimensionalized equivalent stress, hydrostatic pressure, and strain rate satisfy Equation (11):

$$\ln \frac{\sigma^*}{1 + C \ln \dot{\varepsilon}^*} = N \ln(p^* + T^*) + \ln A \quad (11)$$

For ease of calculation, variables *X* and *Y* are defined as shown in Equation (12):

$$\begin{cases} X = \ln(p^* + T^*) \\ Y = \ln \dfrac{\sigma^*}{1 + C \ln \dot{\varepsilon}^*} \end{cases} \quad (12)$$

The variables X and Y exhibit a clear linear relationship, in which N represents the slope of the fitted line and lnA denotes the intercept. The quantitative values for X and Y, derived from the dynamic SHPB experimental response, are systematically summarized in Table 4. It can be seen that the data obtained under impact pressures of 0.5, 0.6, and 0.7 MPa show good mutual consistency, indicating that the dynamic experimental results are reliable and representative. Consequently, the characteristic constitutive parameters were determined to be A=0.53 and N=2.4063.

Table 4 X and Y values obtained from SHPB test results

Sequence Number	&	X	Y
1	230	0.0739	-0.4641
2	396	0.0808	-0.4377
3	510	0.0883	-0.4198

2.2.3.3 Strength model under complete damage condition

Previous investigations have established two primary methodologies for determining the strength parameters in the fully damaged state. On the one hand, an empirical approach involves defining the relationships as *B*=*A*/3 and *M*=*N* [29]. Although this method is characterized by high practical efficiency and computational utility, its limited material-specific precision may adversely affect the predictive accuracy and fidelity of the final constitutive model. On the other hand, a more rigorous methodology utilizes particle confining pressure tests [29] to derive parameters based on the deterministic functional relationship between dimensionless hydrostatic pressure and dimensionless strength.

Owing to its robust experimental foundation, this study adopts the latter approach to ensure a high-fidelity representation of the material's mechanical response. Based on the validated WC-Co cemented carbide data, the failure strength parameters were identified as B = 0.29 and M = 0.67, while the quasi-static tensile strength was experimentally determined as T = 0.95 GPa through Brazilian disc tests [13]. Accordingly, the dimensionless normalized tensile strength was calculated to be $T^* = T / p_{HEl}$ =0.127. The complete set of determined Johnson-Holmquist II (JH-2) constitutive parameters is systematically presented in Table 5.

Table 5 JH2 constitutive model parameters of WC-Co cemented carbide

ρ/(g/cm^3)	G/GPa	T/GPa	K_1/GPa	K_2/GPa	K_3/GPa	σ_{HEL}/GPa	p_{HEL}/GPa
14.2	241	0.95	342	1739	-7228	12.99	7.03

A	B	C	M	N	D_1	D_2	σ_{fmax}

0.53	0.29	0.01043	0.67	2.4063	0.005	1	0.2

3 Removal mechanism of WC-Co cemented carbide

3.1 Criteria and analytical framework for the ductile-to-brittle transition

As shown in Figure 4, the scratching process of a single abrasive grain can be regarded as the local interaction between an individual abrasive and the workpiece during grinding. For the identification of the ductile-regime removal range of WC-Co, the surface morphology of the scratch groove alone is not sufficient, because subsurface damage may occur before visible brittle cracks appear on the scratched surface. Therefore, this section identifies the ductile-regime removal range of WC-Co based on scratching experiments and numerical simulations, providing a basis for the subsequent grinding process.

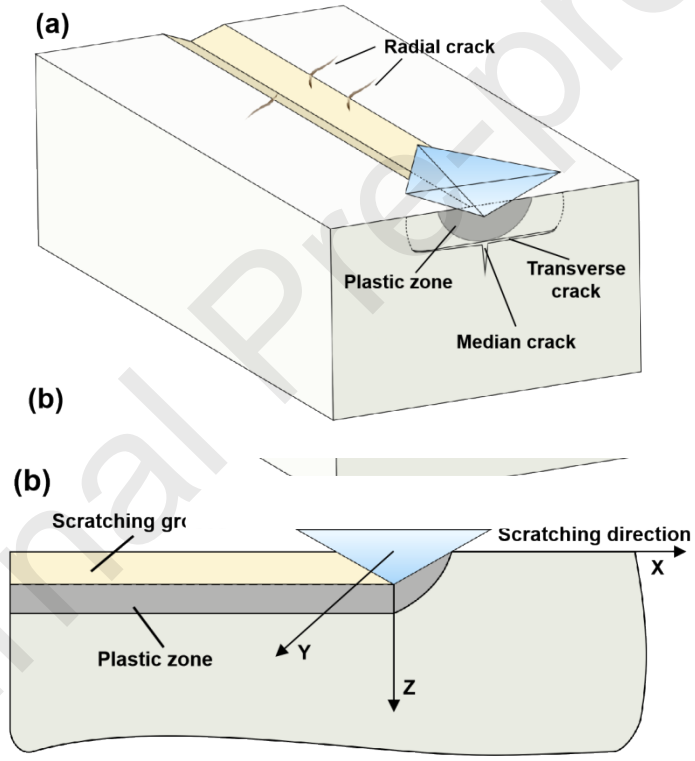

Figure 4 Schematic diagram of single abrasive grain scratch ((a) scratching schematic diagram (b) scratching cross-sectional view)

3.2 Identification of the ductile-regime removal range of WC-Co based on experiments and simulations

Figure 5(a) shows the micro-scratching experiment used to investigate the material-removal behavior of WC-Co cemented carbide, and Figure 5(b) presents the corresponding loading profile. A 120° indenter was employed, and a variable-load scratch with a normal load increasing from 1 to 70 N was conducted along a single scratch path. With the increase in

scratching displacement, the penetration depth increased accordingly. This design makes it possible to examine the evolution of the removal state of WC-Co continuously under different scratching depths within one scratch.

The SEM morphologies at different scratching positions are shown in Figure 5(c–e). In Figure 5(c), the scratch boundary is not obvious, and the removed surface is very smooth. Only a small amount of fine debris particles can be observed inside the scratch groove. In Figure 5(d), no obvious brittle cracks are observed on the removed surface, and the overall surface remains relatively smooth. Meanwhile, the scratch groove becomes much clearer, and the removed material appears as relatively large debris particles that accumulate along the groove boundaries. However, the subsurface damage condition cannot be directly identified from the surface morphology. In Figure 5(e), the scratch damage becomes significantly more severe, and a considerable number of surface cracks can be observed. This indicates that the material-removal mode has shifted from ductile-dominated removal to the brittle-removal stage.

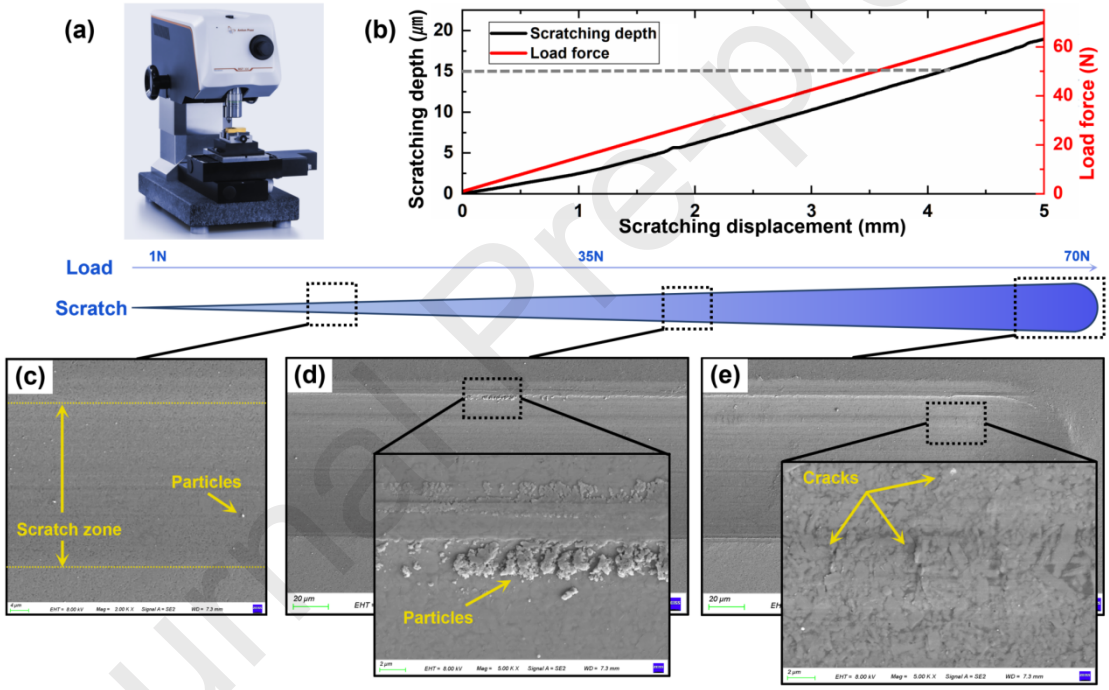

Figure 5 Scratch morphology induced by dynamic loads ((a) scratch tester (b) relationship among scratching displacement, scratching depth and applied load (c-e) SEM images)

Based on the JH-2 constitutive model established in Section 2, finite element simulations of the single-grit scratching process were carried out to analyze the stress evolution and material-removal behavior of WC-Co cemented carbide. In the numerical model, the scratching depth was set to increase continuously from 0 to 15 μm with the displacement of the indenter, so that the change in removal state could be tracked along a single scratching path. To improve computational efficiency, the total scratching displacement was reduced to one tenth of the experimental length while maintaining the depth variation ratio. The WC-Co substrate was

discretized using a structured mesh with an element size of 0.2 µm, and the abrasive grain was modeled as a rigid body.

Figure 6 presents the finite element results of the single-grit scratching process. Figures 6(a)–(d) show the overall evolution of the von Mises stress field with increasing scratching depth. Figure 6(e) gives the top view of the post-scratch stress field and marks two representative locations for further observation of the subsurface damage evolution. In Figure 6(f), when the scratching depth reaches about 8 µm, the removed surface remains relatively regular, but a slight subsurface crack can already be observed at location (1) on the side of the scratch groove. In Figure 6(g), with a further increase in scratching depth, the subsurface crack at location (1) gradually extends. In Figure 6(h), as the scratching depth continues to increase, the subsurface crack at location (1) develops into a surface pit, indicating the occurrence of brittle fracture; meanwhile, a new subsurface crack appears at location (2) near the middle of the groove. In Figure 6(i), the pit at location (1) further enlarges due to brittle fracture, while the crack at location (2) continues to propagate toward the center of the scratch groove.

The simulation results agree well with the scratching experiments in the small-depth range, where the scratched surface remains relatively smooth and the surface quality is still good. In the scratching experiments, distinct brittle cracks are observed on the scratched surface at a depth of 15 µm, whereas in the finite element simulation, subsurface crack initiation can already be identified at about 8 µm. This indicates that subsurface damage occurs earlier than the appearance of visible surface brittle cracks during the scratching process. Therefore, to avoid both subsurface crack initiation and subsequent brittle fracture, the ductile-regime removal window of WC-Co was finally determined as 0-5 µm. It ensures that the subsequent global path planning algorithms can consistently restrict the depth of cut within this safe limit, thereby effectively suppressing subsurface damage

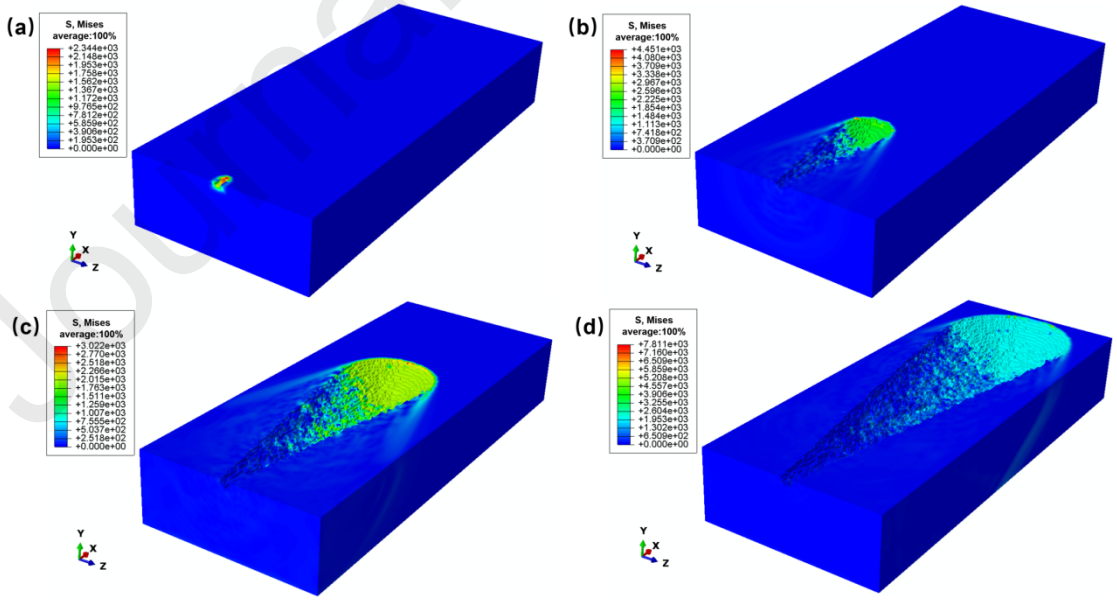

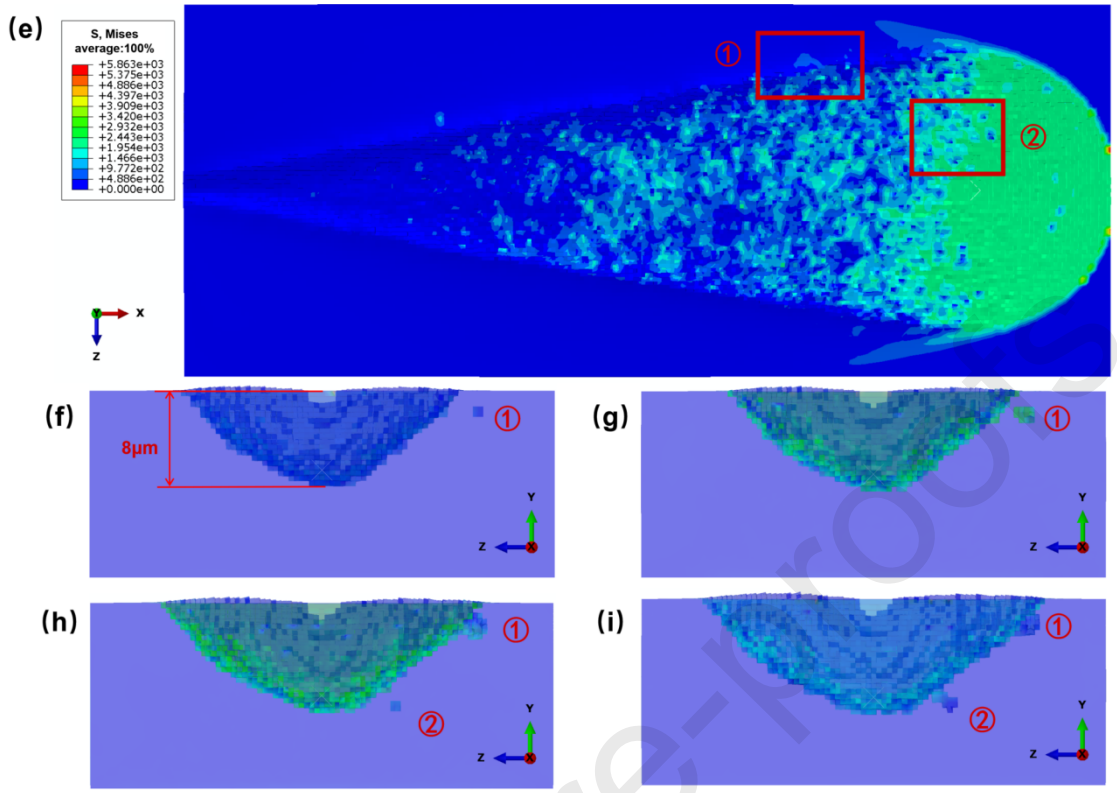

Figure 6 Finite element results of single-grit scratching ((a-d) evolution of Mises stress distribution during scratching, (e) top view of the post-scratch stress field, (f-i) local semi-transparent views of the marked regions in (e) observed along the X-direction)

4 Ultra-precision grinding experiment of sinusoidal cylindrical arrays

4.1 Hybrid grinding strategy and tool preparation

4.1.1 Advantages of hybrid grinding

In the manufacturing of complex microstructured arrays, employing a single grinding technique typically necessitates a compromise between material removal efficiency and form accuracy. Profile grinding wheels excel at high-efficiency bulk material removal. However, their fixed geometric configuration restricts their capacity to rectify localized form deviations. In contrast, ultra-thin arc-shaped wheels demonstrate remarkable efficacy in compensating for local errors, yet they suffer from low efficiency and are susceptible to severe wear when utilized independently for full-scale material removal. Against this backdrop, this study adopts a hybrid grinding strategy that integrates profile grinding and ultra-thin wheel compensation, aiming to synergize high-efficiency shaping with high-precision corrective machining.

4.1.2 Preparation and wear detection of formed grinding wheels

The grinding tool utilized in this investigation is a SDC1000N100B5 type wheel. Dressing of the profile wheel is executed utilizing a specialized electroplated dressing tool, as systematically illustrated in Figure 7(a). This dressing wheel incorporates dual sinusoidal profile regions, which

facilitate multiple reconditioning cycles to maintain the topographical precision and geometric fidelity of the formed wheel. For the experimental setup, the specimens are rigidly secured to the *C*-axis rotary table using epoxy resin, allowing for precise modulation of the feed orientation via *C*-axis rotation. The kinematic configuration of the precision grinding system involves the *Y*-axis and *Z*-axis for the deterministic control of feed velocity and grinding depth, respectively, while the *X*-axis governs the lateral positioning of the grinding zone. Furthermore, to reduce thermomechanical damage during grinding, a fully synthetic water-based grinding fluid was used as the coolant at a concentration of 3%, with a nozzle flow rate of 9 L/min.

The feedback of the follow-up errors of several axes of the entire machine tool is generally within 5 nm. The precision of vertical alignment is approximately 300 nm. In terms of roundness accuracy, it is achieved by using an external sigma dynamic balancing instrument and is approximately 2 nm. The radial stiffness of the grinding shaft is 180 N/μm, and the axial stiffness is 250 N/μm. The above-mentioned hardware precision ensures the accuracy of the ultra-precise grinding of the contour.

The amplitude of the sinusoidal curve is 150 μm, so the theoretical total processing depth is 300 μm. Considering machine errors and initial surface quality, the total depth is adjusted to 320 μm with 3 processing cycles. The graphite workpiece was ground separately using the profile grinding wheel before and after grinding in Figure 7(b), so as to obtain the surface profile characteristics of the wheel. Figure 7(c) shows the surface profile measurement results of the profile grinding wheel before and after grinding. It can be observed that the sinusoidal cylindrical array profile achieves a precise replication of the profile grinding wheel profile, and no excessive wear occurred on the wheel during the grinding process. The minimal wear amount verifies the practicality of the profile grinding wheel in the batch machining of optical molds.

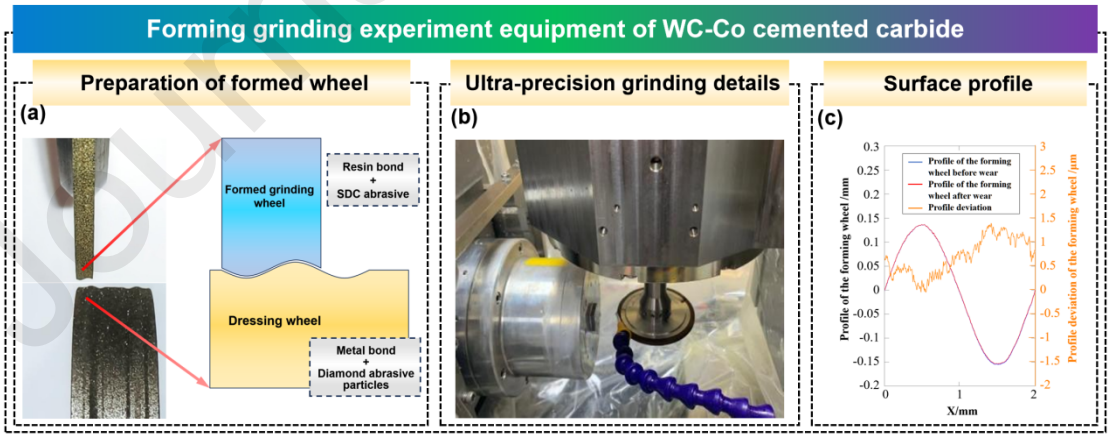

Figure 7 Processing area diagram

((a) schematic diagram (b) physical diagram (c) surface profile)

4.1.3 Preparation and in-situ dressing of ultra-thin grinding wheels

The arc radius within the active grinding zone is the pivotal dimension for ultra-thin wheels, necessitating a strategic balance between profile curvature and tool wear kinetics. An excessively small radius induces accelerated wear and structural deformation, compromising the wheel's geometric stability. Based on established research [30], the selection of the arc radius is constrained to $R>0.2$. Furthermore, curvature analysis indicates that the minimum radius of curvature is localized at the troughs of the sinusoidal profile, defining the critical geometric constraint for the precision grinding process.

$$\rho = \left| \frac{(1+f'(x)^2)^{\frac{3}{2}}}{f''(x)} \right| = \left| \frac{(1+0.0225\pi^2\cos^2(\pi x))^{\frac{3}{2}}}{0.15\pi^2\sin(\pi x)} \right| . \quad (13)$$

The minimum radius of curvature occurs at the wave trough, calculated as ρ_{min} = 0.675 mm. To prevent geometric interference, the wheel's arc radius must remain below this threshold. Accounting for fabrication feasibility, wear resistance, and grinding precision, the arc radius for the ultra-thin grinding wheel was finalized at R 0.6 mm.

Figure 8(a-b) shows the motion trajectory of the dressing wheel relative to the workpiece in the dressing system. The dressing wheel moves at a certain speed, with its center coordinates at (x_0, y_0, z_0), and the center coordinates of the vertical grinding wheel at ($x_{0'}$, $y_{0'}$, $z_{0'}$). The motion trajectory equation of the grinding wheel edge is f(x, y).

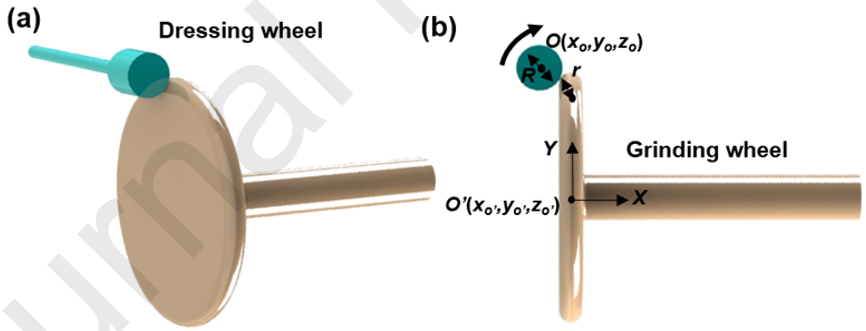

Figure 8 Schematic diagram of in-situ dressing for ultra-thin grinding wheel((a) The dressing system (b) the motion trajectory of the dressing wheel)

4.2 Ultra-thin grinding wheel compensation grinding path planning

4.2.1 Ultra-thin grinding wheel curved surface forming method

In the proposed generating method, the grinding wheel first feeds along the Y-axis to complete one full longitudinal pass, completes the grinding in the entire Y-axis direction, and then moves a certain step length along the X-axis and Z-axis before feeding again along the Y-axis, as shown in Figure 9(a). Since the head of the grinding wheel is circular, there will be unground areas between adjacent grinding paths. The schematic diagrams of the unground

areas produced by the two methods are shown in Figure 9(b). Sinusoidal cylindrical arrays on WC-Co cemented carbide molds are first generated by profile grinding. The effects of various generation and path planning methods on surface quality are explored. Then a global wheel path planning strategy based on equal material removal rate is proposed. Ultra-thin arc wheel compensation grinding experiments were carried out, and related algorithms are integrated to significantly improve processing efficiency while ensuring surface accuracy of sinusoidal cylindrical arrays.

Traditional grinding of cylindrical arrays often employs layer-by-layer removal, which is characterized by excessive tool idling and significant energy waste. In contrast, this study implements a sequential trajectory-based strategy, where each path is ground to full depth individually, enhancing efficiency and allowing for flexible parameter modulation, as shown in Figure 9(c). Ultra-thin arc wheels, characterized by high dimensional precision and superior surface integrity, are versatile for diverse machining applications. The fillet radius in the active grinding zone is established at *R* 0.6 mm. A D2000N100B5 diamond wheel is utilized, featuring a 40 mm diameter and a 2000# grit size. To ensure beam parallelism during transmission, sinusoidal cylindrical array lenses demand stringent profile accuracy. A *Y*-axis feeding strategy is implemented: following a complete longitudinal stroke, incremental steps are taken along the *X* and *Z* axes. This trajectory ensures metrological continuity of the machined surface along the cylindrical *Y* direction.

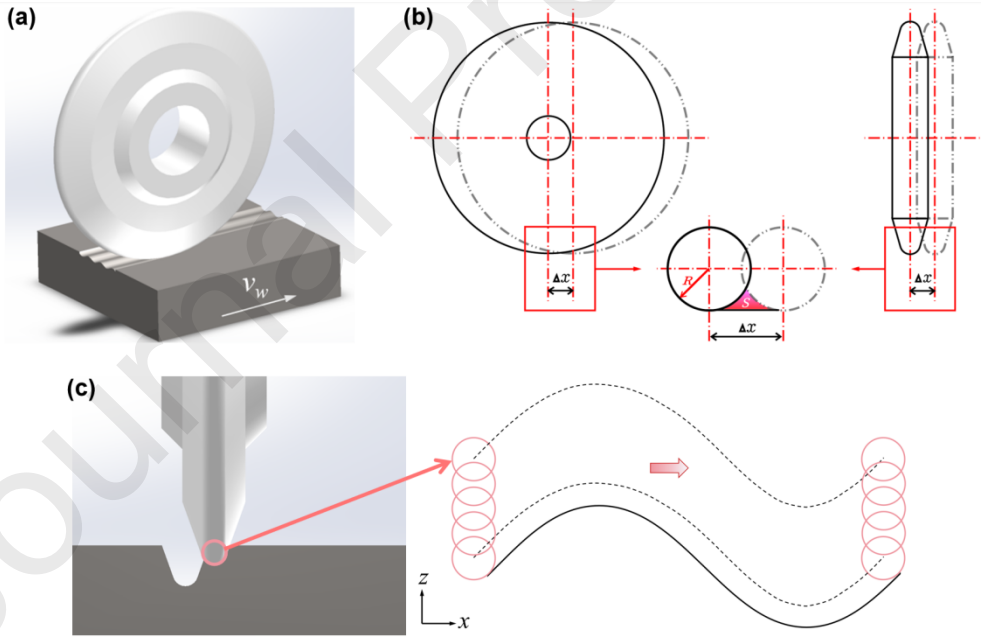

Figure 9 Schematic diagrams of generative method((a) The generative form (b) The ungrounded areas produced by the two methods (c)single-trajectory full-depth grinding method)

4.2.2 Single-layer path planning for ultra-thin wheels

Arc wheel envelope grinding is widely utilized for fabricating complex curved surface arrays, where step configuration is critical to surface quality. Common path planning strategies

include equal step, equal arc length, and equal residual height. As illustrated in Figure 10(b), residual height *h* (scallop height) represents the elevation of uncut material between adjacent tool trajectories. Equal residual height planning ensures a uniform distribution of these peaks across the surface. The analytical expression for residual height *h* is defined as:

$$h = r_\theta - \sqrt{r_\theta^{\,2} - \frac{d^2}{2}} \quad (14)$$

where r_ϑ is the curvature radius of the near-arc section wheel, and *d* is the distance between centers O_n and O_{n+1} of adjacent trajectory grinding areas. When the previous grinding path was being made by the grinding wheel, the point of tangency $M_j(x_{Mj}, z_{Mj})$ between the arc-shaped grinding wheel head and the curved surface was calculated. The normal line at this point on the curve passed through the center of the arc-shaped grinding wheel $O_j(x_{Oj}, z_{Oj})$. The distance from the center of the circle to the point of tangency is equal to the radius *r* of the grinding wheel.

Let the center of the grinding wheel during the grinding of the latter grinding path be $O_{j+1}(x_{Oj+1}, z_{Oj+1})$, and the point of tangency with the curve be $M_{j+1}(x_{Mj+1}, z_{Mj+1})$. The arc contour of the wheel's grinding area for two adjacent grinding paths intersects at a point, which is $N_j(x_{Nj}, y_{Nj})$. Draw a perpendicular line from point N_j to the curve, and let the foot of the perpendicular be D_j. Then, the length of the line segment N_jD_j is the residual height *h*.

According to the illustrated coordinate system, the equation of the arc contour of the grinding wheel during the previous grinding operation is:

$$(x - x_{O_j})^2 + (z - z_{O_j})^2 = r^2 \quad (15)$$

Point N_j is located on the circumference of the grinding wheel contour at the previous grinding path. Therefore, the coordinates of point N_j satisfy the following circular formula:

$$(x_{N_j} - x_{O_j})^2 + (z_{N_j} - z_{O_j})^2 = r^2 \quad (16)$$

Point D_j is the foot of the perpendicular from point N_j to the curve. Therefore, the coordinates of point N_j can be obtained from the coordinates of point D_j, as shown in Equation (17). The sign of the slope of the curve at point D_j will affect the calculation method of the coordinates of point D_j.

$$(x_{N_j}, z_{N_j}) = \begin{cases} (-\dfrac{h}{\sqrt{1+f'(x_{D_j})^2}} + x_{D_j}, (-\dfrac{f'(x_{D_j})\cdot h}{\sqrt{1+f'(x_{D_j})^2}} + f(x_{D_j})), & f'(x_{D_j}) \geq 0 \\ (\dfrac{h}{\sqrt{1+f'(x_{D_j})^2}} + x_{D_j}, (\dfrac{f'(x_{D_j})\cdot h}{\sqrt{1+f'(x_{D_j})^2}} + f(x_{D_j})), & f'(x_{D_j}) < 0 \end{cases} \quad (17)$$

Since the coordinates are known, the simultaneous equations (16) - (17) can be used to obtain the coordinates of point D_j and point N_j. Point N_j lies on the wheel contours corresponding to two adjacent grinding paths. Therefore, its coordinates satisfy the following formula:

$$(x_{N_j} - x_{O_{j+1}})^2 + (z_{N_j} - z_{O_{j+1}})^2 = r^2 \quad (18)$$

The center of the circle O_{j+1} is taken as the point M_{j+1} as the tangent point with the curve, and its coordinates can be expressed as:

$$(x_{O_{j+1}}, z_{O_{j+1}}) = \begin{cases} (-\dfrac{r}{\sqrt{1+f'(x_{M_{j+1}})^2}} + x_{M_{j+1}}, (-\dfrac{f'(x_{M_{j+1}})\cdot r}{\sqrt{1+f'(x_{M_{j+1}})^2}} + f(x_{M_{j+1}})), & f'(x_{M_{j+1}}) \geq 0 \\ (\dfrac{r}{\sqrt{1+f'(x_{M_{j+1}})^2}} + x_{M_{j+1}}, (\dfrac{f'(x_{M_{j+1}})\cdot r}{\sqrt{1+f'(x_{M_{j+1}})^2}} + f(x_{M_{j+1}})), & f'(x_{M_{j+1}}) < 0 \end{cases} \quad (19)$$

Simultaneously solving Equations (18–19) yields the spatial coordinates for points O_{j+1} and M_{j+1}. Through this iterative procedure, the complete trajectory for the arc-profile wheel is established under the equal residual height algorithm. The process terminates once the *x*-coordinate of the tangency point exceeds the prescribed boundary, signaling the completion of the grinding pass. This single-layer path planning approach is consistently applied to each material removal stage. The corresponding algorithmic logic and kinematic schematics are systematically detailed in Figure 10(a) and Figure 10(b–c), respectively.

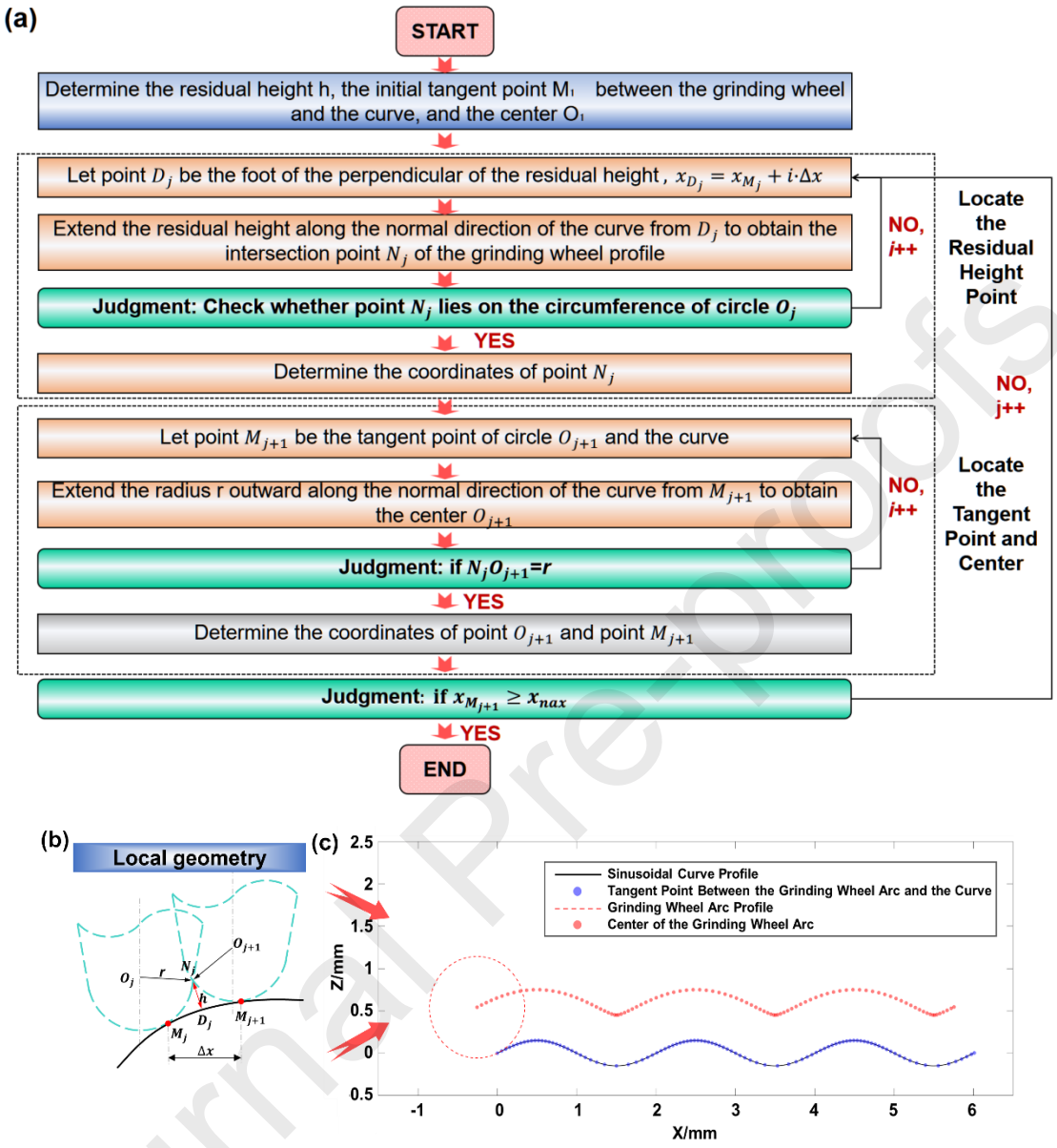

Figure 10 Single-layer path planning for ultra-thin wheels ((a) residual height planning algorithm (b) equal residual height method (c) constant scallop height method path planning)

To balance processing efficiency and surface integrity, 300 grinding trajectories are selected, corresponding to a residual height of h=8.42×10^{-5} mm. The center-point trajectory of the arc-profile wheel is illustrated in Figure 10(c) (simplified to 100 paths for visual clarity). This equal residual height planning ensures a uniform distribution of residual peaks and balanced contact point trajectories. Furthermore, maintaining a consistent material removal rate is critical for mitigating defects such as surface scratches, thermal burns, and waviness while prolonging tool life. As shown in Figure 11(a), material removal rate represents the volume of material dislodged per unit time, which is analytically determined according to Equation (20) [31]31]:

$$Z_w = S_w \cdot v_w \quad (20)$$

Where S_w denotes the projected area of the wheel-workpiece contact zone on the *x*-*z* plane. Based on prior surface integrity analysis, the projected area exhibits high longitudinal uniformity along the *Y*-axis. Figure 11(b) reveals that the variation range of *Sw* under the constant residual height strategy is relatively narrow, which effectively mitigates *Sz* discrepancies typically induced by varying residual heights on concave and convex topographies. Therefore, the single-layer path planning algorithm implemented in this study successfully fulfills the stringent precision requirements for WC-Co substrate processing.

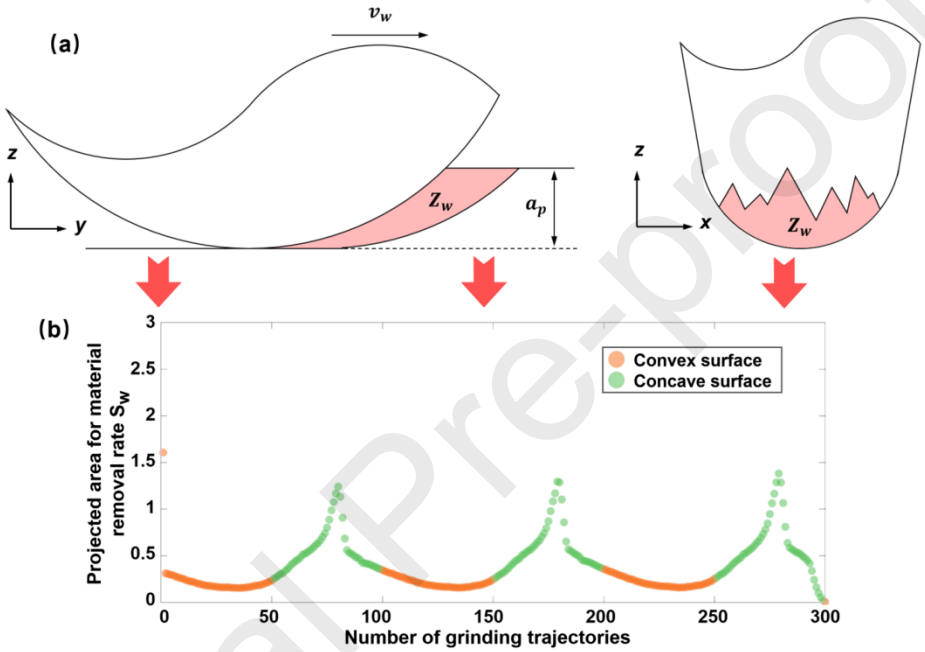

Figure 11 Analysis of material removal rate ((a) schematic diagram of material removal rate (b) the projected area Sw of material removal rate along the grinding trajectory)

4.2.3 Global path planning for ultra-thin wheels

Compensation grinding utilizing ultra-thin arc wheels is performed post-forming. Since form errors fluctuate across the surface, a uniform depth of cut (DoC) fails to ensure consistent material removal, often triggering stochastic grinding forces, vibration, or brittle chipping. To mitigate this, a global path planning algorithm based on a constant material removal rate is adopted. This approach ensures homogeneous thermal and mechanical loads, resulting in uniform wheel wear. The material removal rate for each pass is calculated based on the target profile and wheel radius; any non-integer residual material is integrated as the initialization parameter for each trajectory to safeguard final surface integrity. The specific algorithmic logic is illustrated in Figure 12.

The computational toolpath lattice is determined via the proposed algorithm, with the initial grinding trajectory illustrated in Figure 13(a). By setting the projected area S_w to 1.3×10^{-4}

mm², 13 longitudinal passes are required for complete material removal. As the removal width progressively increases from the crest to the root, the DoC is adaptively reduced to maintain a constant removal rate; the DoC graduates from an initial 1.18 μm to a final 0.86 μm, staying within the optimized range for suppressing tool wear and ensuring surface integrity. The corresponding trajectory for the second pass is depicted in Figure 13(b). Due to the volumetric reduction from the preceding trajectory, the requirement is reduced to 3 passes. In this stage, the DoC ranges from 2 μm to 1.26 μm, which effectively maintains the material removal efficiency while operating within the ductile-regime machining limits necessary for high-precision WC-Co surfaces.

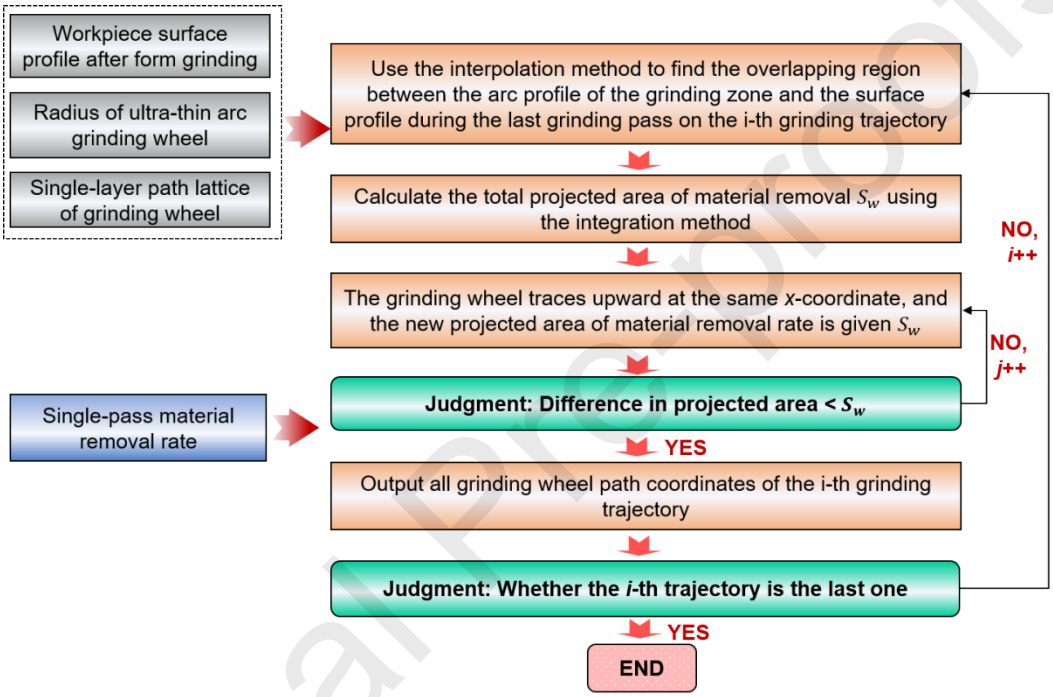

Figure 12 Algorithm flow chart for material removal rate

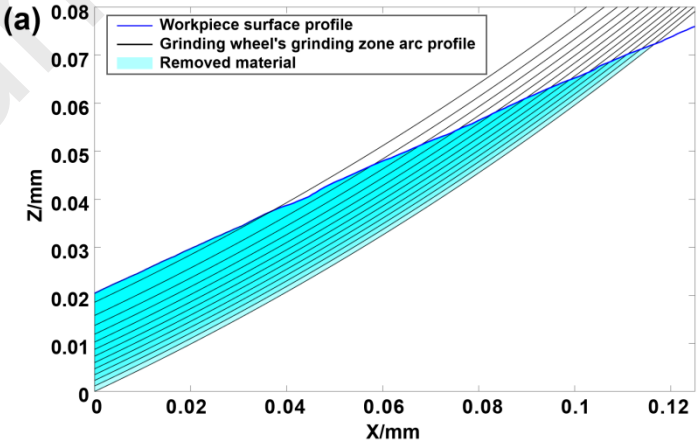

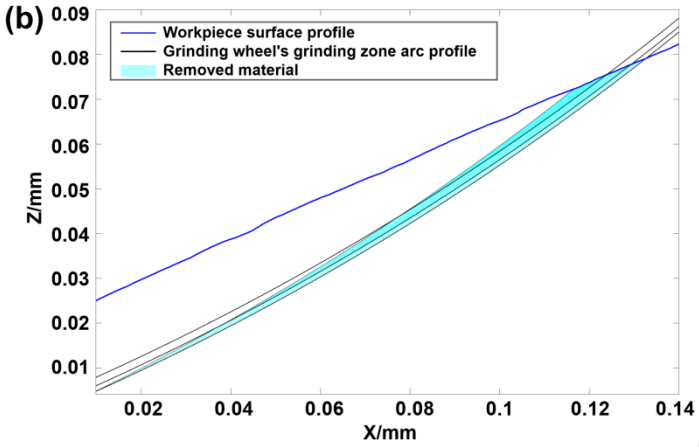

Figure 13 The entire grinding wheel path of ((a) the first (b) the second grinding trajectory)

The final-pass grinding depth for each trajectory is illustrated in Figure 14(a), ranging from 0.37 μm to 2.15 μm to ensure uniform surface integrity. Distinctions in depth between convex and concave topographies are evident. The scatter plot in Figure 14(b) elucidates the stochastic relationship between grinding depth and the cumulative number of passes across all toolpaths. Notably, the depth of cut on convex surfaces generally exceeds that on concave surfaces. This is primarily because the extended tool-workpiece contact length on concave geometries necessitates a reduced depth to maintain a constant material removal rate. Furthermore, all calculated depths remain within the 0–5 μm ductile-regime operational window established in Section 3. This strategy effectively optimizes material removal efficiency while precluding brittle fracture damage, thereby satisfying the stringent requirements for high-precision surface finish on WC-Co substrates.

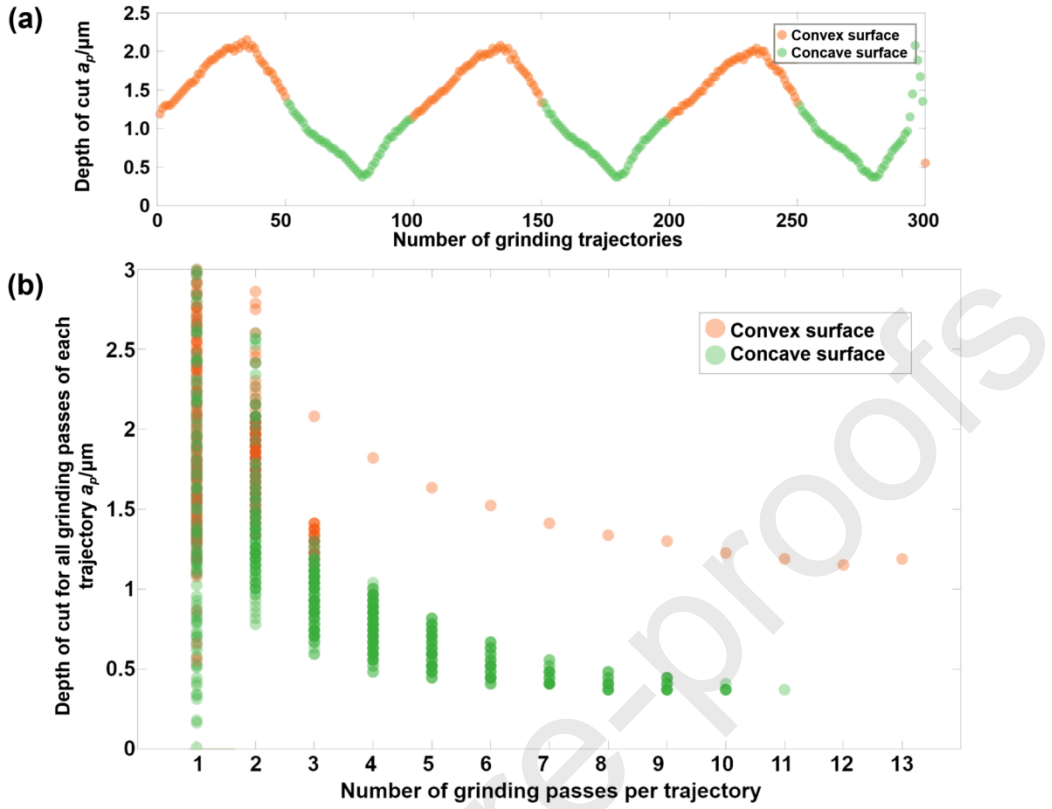

Figure 14 Grinding depth distribution ((a) the grinding depth of each grinding trajectory when closest to the surface (b) the full grinding depth of each grinding trajectory)

4.3 Experimental results of hybrid grinding process

4.3.1 Results of formed wheel grinding

Surface integrity of the generated cylindrical arrays is systematically evaluated based on form accuracy and surface roughness. Form error, characterizing the metrological deviation from the ideal geometric profile, is illustrated in Figure 15(b). The cumulative form error over three sequential grinding cycles reached a PV magnitude of 18.51 μm, with a mean PV value of 17.36 μm. It is substantiated that the form deviation exhibits a progressive expansion with increasing grinding cycles. This non-uniform error distribution along the ordinate is primarily attributed to the spatial variation in grinding heights inherent to the sinusoidal contour, which induces localized intensification of abrasive wear at specific tool-workpiece contact zones. This trend demonstrates robust consistency with the deterministic wear patterns of the profile grinding wheel, substantiating a high degree of replication fidelity without signs of catastrophic surface damage. Furthermore, to quantify the profile fidelity, the surface profile deviation of the WC-Co substrate was rigorously characterized utilizing a Panasonic UA3P 500H contact profilometer, as depicted in Figure 15(c).

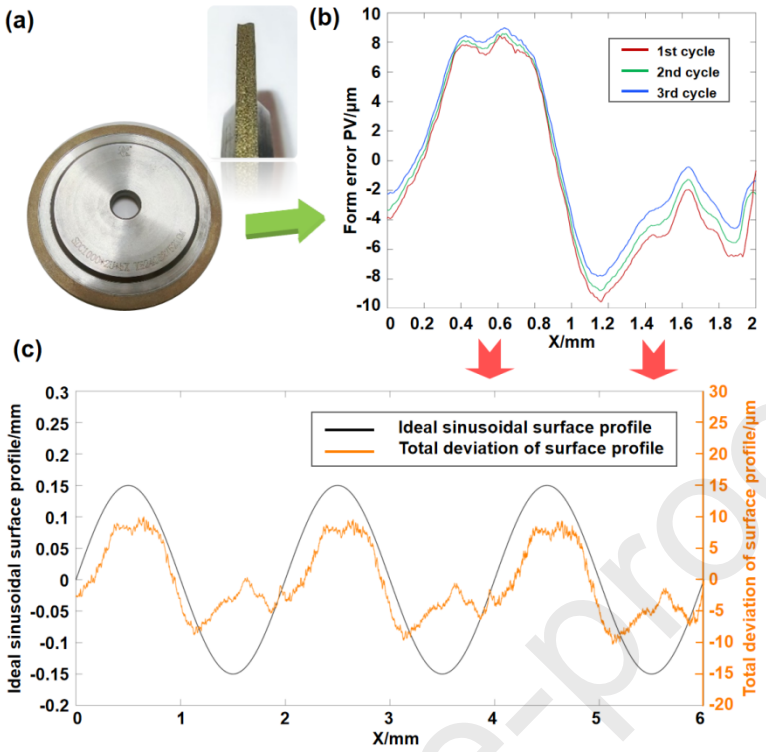

Figure 15 Grinding with the formed grinding wheels ((a) sinusoidal curve formed grinding wheel (b) total profile deviation after forming grinding (c) surface shape error)

The surface roughness of the WC-Co array after profile grinding is presented in Figure 16. To evaluate the topographical uniformity, spatial sampling was systematically conducted at the peaks, slopes, and troughs of each grinding cycle. The experimental results demonstrate a relatively homogeneous distribution across the array, although a progressive intensification in roughness is observed from the peaks toward the troughs. This phenomenon is primarily attributed to the kinematic interaction where the workpiece troughs correspond to the peaks of the profile grinding wheel, resulting in accelerated abrasive wear and intensified localized contact during the material removal process. This trend is consistent with the previously observed form error evolution and wheel wear pattern. Quantitatively, the surface finish attains Grade 11 post-grinding and improves to Grade 12 following simulated polishing, effectively meeting the technical specifications for specific optical applications. Although profile grinding wheel machining has already established the fundamental sinusoidal cylindrical array with acceptable form accuracy and surface quality, the residual deviations indicate that further corrective machining is still necessary. Therefore, ultra-thin wheel compensation grinding is subsequently introduced on this pre-generated surface to inherit the overall profile and further suppress the remaining local form and surface errors.

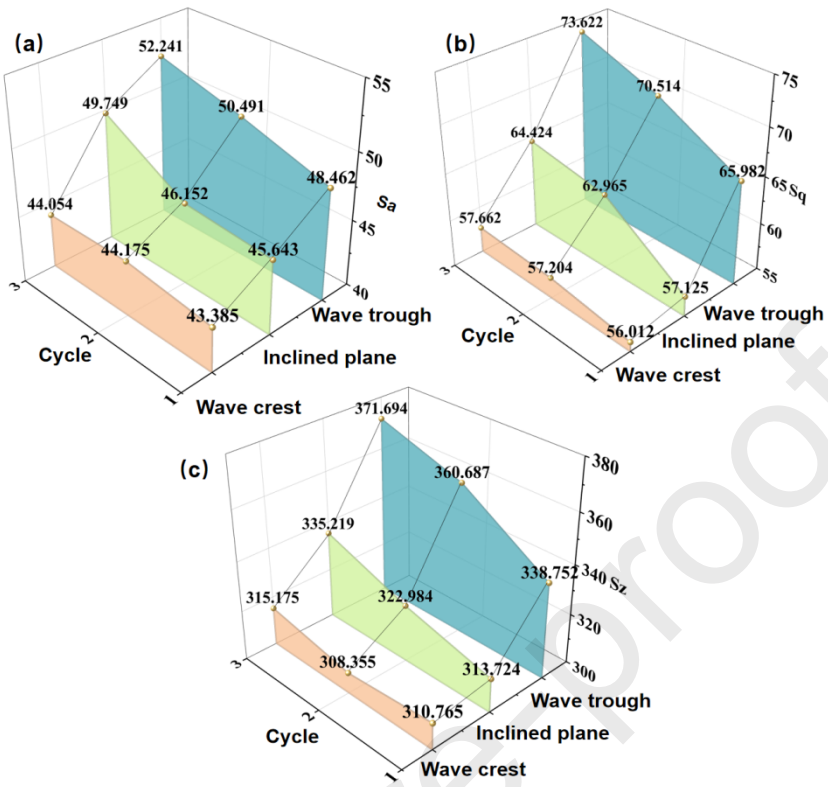

Figure 16 Surface roughness of workpiece after forming grinding ((a) *Sa* (b) *Sq* (c) *Sz*)

4.3.2 Results of ultra-thin grinding wheel grinding

After profile grinding, the workpiece already exhibited a well-formed macro-profile, providing a favorable basis for subsequent ultra-thin wheel compensation grinding. The experimental setup adopted for compensation grinding was identical to that employed in the profile grinding wheel grinding process, maintaining consistent wheel speed (v_s=21m/s) and workpiece feed rate (v_w=100 mm/min) to ensure comparable surface quality. The grinding depth (a_p) was compensated according to the measured surface contour after profile grinding wheel grinding and a global path planning strategy designed to achieve uniform material removal rate.

Precise tool setting prior to compensation grinding is essential to minimize secondary clamping errors arising from offline measurements and wheel replacement. Before removing the profile grinding wheel, a micro-groove of 2 μm depth was ground on the planar region of the workpiece using the convex surface of the wheel. The lateral displacement between the lowest point of this groove and the nearest peak of the sinusoidal array was subsequently measured using a white light interferometer. After installing the ultra-thin wheel, another 2 μm-deep micro-groove was ground at a predetermined distance from the previous groove created by the profile grinding wheel. The lateral displacement between the lowest points of the two grooves was then measured using a confocal displacement sensor, enabling calculation of the distance from the ultra-thin wheel groove to the starting position of the sinusoidal array according to Equation (21):

$$\Delta x = \Delta x_1 + \Delta x_2 - \frac{T}{2} \quad (21)$$

where *T* is the period of the sinusoidal curve. The surface profile deviation after ultra-thin arc wheel compensation grinding is shown in Figure 17(a). The integer multiple of trajectories to the period ensures consistent contour error trends across cycles, guaranteeing uniformity.

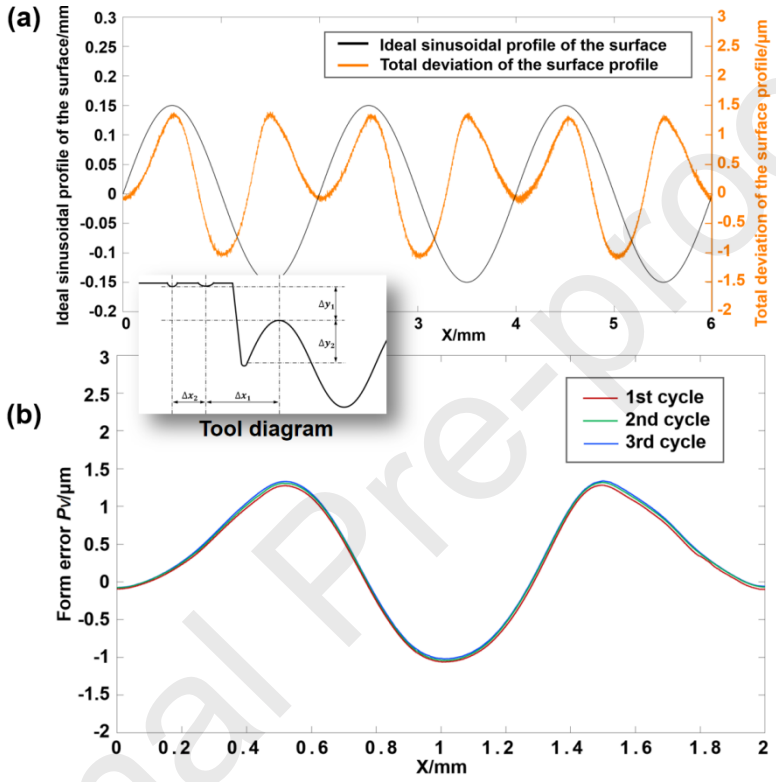

Figure 17 Compensatory grinding results((a) total deviation of surface profile (b) form error)

The form error following compensation grinding, as depicted in Figure 17(b), achieved a PV value of 2.43 μm overall, with an average PV of 2.34 μm across three cycles. In comparison, the corresponding values after profile grinding wheel machining were 18.51 μm and 17.36 μm, respectively. This indicates that the ultra-thin wheel compensation process effectively inherited the pre-generated array profile while markedly suppressing the residual local form deviations left by profile grinding wheel machining. The consistency of the errors across the cycles validates the effectiveness of the path planning strategy. As compensation grinding was conducted on the surface produced by post-forming wheel grinding, the total material removal volume was significantly lower than that when using ultra-thin wheels alone, thereby reducing wheel wear, improving surface quality, and decreasing wheel dressing frequency, thus enhancing overall practicality. Surface roughness measurements were performed on the workpiece, with sampling positions chosen at the wave crest, slope, and valley of each cycle, as shown in Figure 18.

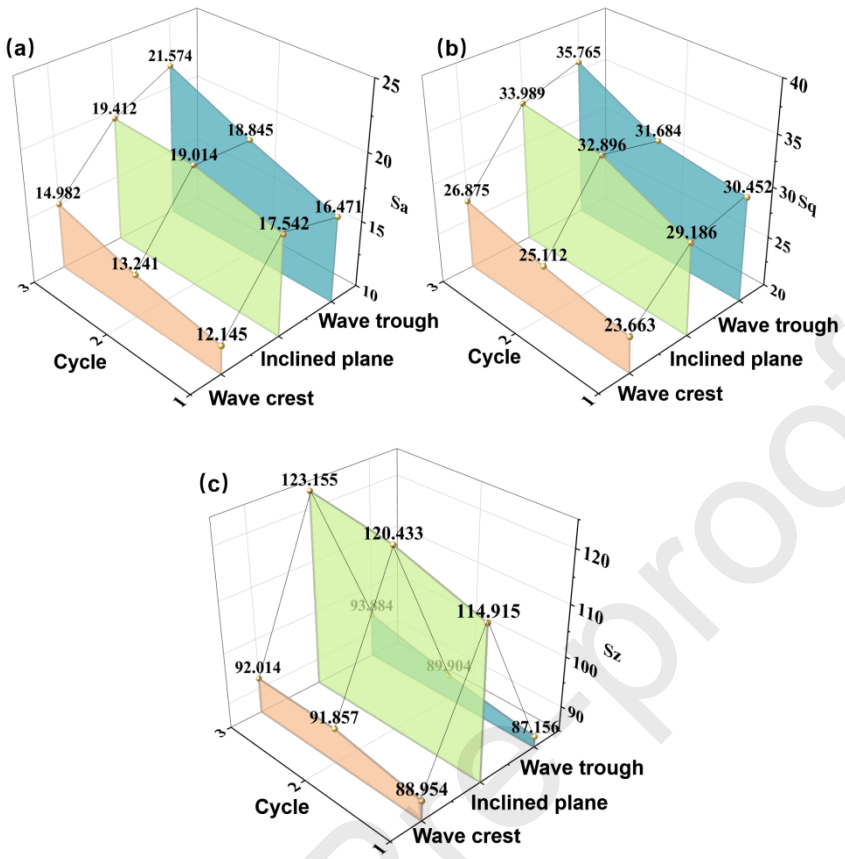

Figure 18 Surface roughness of WC-Co cemented carbide workpiece after compensation ((a) *Sa* (b) *Sq* (c) *Sz*)

The surface roughness after compensation grinding exhibited high uniformity, as shown in Figure 19. The Sz parameter was greater on the slopes than at the peaks and troughs, mainly because the actual residual height was projected more strongly onto the Z-axis owing to the steeper local slope angles. This tendency is consistent with the earlier estimation of residual height under the equal-scallop-height path planning strategy. Therefore, for the intended application scenario of this study, the obtained Sz level remains acceptable. The troughs exhibited slightly higher roughness than the peaks because convex surface grinding involved smaller depths of cut. Although surface roughness showed no strong correlation with grinding depth, it increased marginally as depth increased. Nevertheless, the uniform material removal rate promoted consistent removal uniformity, leading to overall uniform roughness across the surface. The roughness cloud map of the second cycle is presented, revealing favorable surface condition characterized by excellent overall uniformity. FFT low-pass filtered roughness cloud maps of the peaks, slopes, and troughs indicated that surface roughness attained grade 13 after compensation grinding and grade 14 after simulated polishing, thus fulfilling the precision requirements for sinusoidal cylindrical structure array molds and lenses.

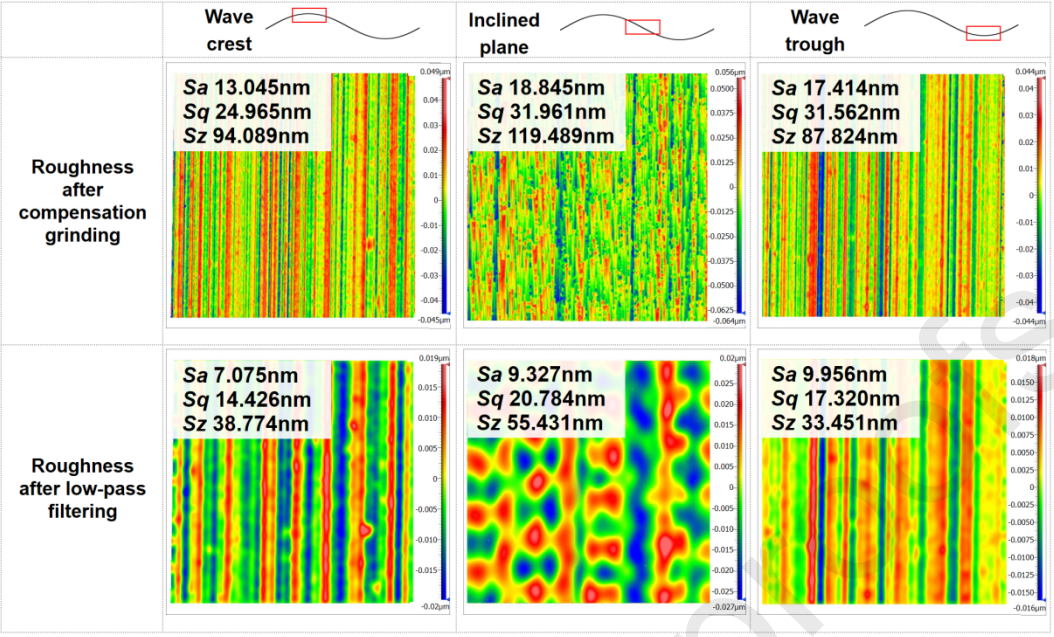

Figure 19 Surface roughness cloud at different positions

5 Conclusion

To investigate the material behavior, removal characteristics, and surface-generation control of WC-Co cylindrical array molds, quasi-static and dynamic SHPB tests were conducted to calibrate the JH-2 constitutive model. Single-abrasive scratching experiments and simulations were performed to identify the ductile-regime removal window. On this basis, a hybrid grinding strategy integrating profile generation, deterministic compensation, and removal-consistent path planning was developed for the high-precision and low-damage manufacturing of sinusoidal cylindrical array molds.The primary conclusions are as follows:

(1) Through quasi-static and dynamic mechanical testing, a calibrated JH-2 constitutive model for WC-Co cemented carbide was developed. This model effectively captures the high-strain-rate mechanical response of WC-Co during ultra-precision grinding, thereby laying a fundamental constitutive foundation for investigating its material removal mechanisms and dynamic damage evolution processes.

(2) Single-abrasive scratch tests and finite element simulations were used to identify the ductile-regime removal window of WC-Co cemented carbide. The results indicate that subsurface crack initiation occurs at about 8 μm in simulation, while visible brittle cracks appear at 15 μm in the experiments. Accordingly, the depth-of-cut range of 0-5 μm was determined as the ductile-regime process window for WC-Co to suppress subsurface damage in precision grinding.

(3) A hybrid grinding strategy was proposed for fabricating sinusoidal cylindrical arrays, integrating high-efficiency profile shaping via a profile diamond grinding wheel with

deterministic form correction using an ultra-thin diamond wheel. The machined array mold achieved PV value of 2.43 μm and *Sa* value of 17.025 nm, demonstrating excellent morphological uniformity across the entire structure.

(4) When combined with an equal-residual-height toolpath and a global path planning method based on constant material removal rate, this hybrid strategy realizes stable ductile-regime material removal, significantly enhances form accuracy, and preserves nanoscale surface integrity of the machined components.

References

[1] Peixoto C, Valentim P, Sousa P, et al. Injection molding of high-precision optical lenses: A review[J]. Precision Engineering, 2022, 76: 29-51.

[2] Lu S, Cao Z, Ling J, et al. Recent Progress in Liquid Microlenses and Their Arrays for Adaptive and Applied Optical Systems[J]. Micromachines, 2025, 16(10): 1158.

[3] Zhong L, Liu W, Gong H, et al. Electrohydrodynamically Printed Microlens Arrays with the High Filling Factor near 90%[J]. Photonics, 2025, 12(5): 446.

[4] Hajj T, Bigot L, Pastre A, et al. Optically Aligned Molded Microlens Arrays on Multi-Core Fibers for Sub-Wavelength Focusing[J]. Journal of Lightwave Technology, 2025, 43(10): 4928-4933.

[5] Zhang Y, Liang R, Spires O, et al. Precision glass molding of diffractive optical elements with high surface quality[J]. Opt Lett, 2020, 45(23): 6438-6441.

[6] Tang X, Wang Z, Huang L, et al. Preparation, properties and microstructure of high hardness WC-Co cemented carbide tool materials for ultra-precision machining[J]. International Journal of Refractory Metals and Hard Materials, 2023, 116: 106356.

[7] Sun S, Li K, Chu W, et al. Tungsten carbide molds for precision glass molding process: Mechanism of high-temperature degradation[J]. International Journal of Refractory Metals and Hard Materials, 2022, 105: 105841

[8] Zhang S, Zhou Y, Zhang H, et al. Advances in ultra-precision machining of micro-structured functional surfaces and their typical applications[J]. International Journal of Machine Tools and Manufacture, 2019, 142: 16-41.

[9] Li S, Wu C, Chen L, et al. Investigations on the material removal and damage formation mechanisms of WC-Co cemented carbide in hybrid laser softening and single-grain scratching processes[J]. Tribology International, 2026, 214(part A): 111129.

[10] Wu C, Li B, Pang J, et al. Ductile Grinding of Silicon Carbide in High Speed Grinding[J]. Journal of Advanced Mechanical Design Systems and Manufacturing, 2016, 10(2):JAMDSM0020.

[11] Duszová A, Halgaš R, Bľanda M, et al. Nanoindentation of WC–Co hardmetals[J]. Journal of the European Ceramic Society, 2013, 33(12):2227-2232.

[12] Liu Y, Wang J, Gu Y, et al. Research of brittle-plastic behavior of SiCp/Al composites based on nano-indentation/scratch[J]. Diamond & Abrasives Engineering, 2024, 44(5): 607-620.

[13] Gao Y, Wang K, Huang W, et al. Dynamic constitutive relation and macro/micro failure mechanism of fine-grained WC-Co composite[J]. International Journal of Refractory Metals and Hard Materials, 2024, 124: 106856.

[14] Jia X, Zhang Z, Li X, et al. Compressive properties and failure mechanisms of AlON ceramics under different strain rates[J]. Ceramics International, 2024,50(8),12787-12801.

[15] Zhao L, Zhang J, Pfetzing J, et al. Depth-sensing ductile and brittle deformation in 3C-SiC under Berkovich nanoindentation[J]. Materials & Design, 2021, 197:109223.

[16] Beaucamp A, Kirsch B, Zhu W. Advances in grinding tools and abrasives[J]. CIRP Annals, 2022, 71(2): 623-646.

[17] Butler S, Axinte D, Daine M. Solid diamond micro-grinding tools: From innovative design and fabrication to preliminary performance evaluation in Ti-6Al-4V[J]. International Journal of Machine Tools & Manufacture, 2012, 59:55-64.

[18] Zhang J, Zheng Y, Li Y, et al. Compressive failure and fragmentation of fused silica glass under quasi-static loading[J]. Journal of Non-Crystalline Solids, 2024, 641: 123112

[19] Wu Q, Deng Z, Pan Z, et al. Preparation and Grinding Surface-quality of a New Diamond Fiber Wheel[J]. Journal of Mechanical Engineering, 2014, 50(11): 205-212.

[20] Chen S, Lin S. Development of an extremely thin grinding-tool for grinding microgrooves in optical glass[J]. Journal of Materials Processing Technology, 2011,211(10):1581-1589.

[21] Pimenov D, Silva L, Kuntoğlu M, et al. Review of advanced sensor system applications in grinding operations[J]. Journal of Advanced Research, 2025, 77: 371-405.

[22] Guo P, Wei Z, Zhang S, et al. Feature-adaptive toolpath planning with enhanced surface texture uniformity for ultra-precision diamond milling of freeform optics[J]. Journal of Materials Processing Technology, 2024, 323: 118220.

[23] Liu J, Li X, Li Y, et al. Grinding Paths freely program in the tool grinding system[J]. Manufacturing Technology & Machine Tool, 2020, (5): 159-162.

[24] Wu C, Shi J, Li T, et al. A Point Cloud Registration Method Based on Point-to-Triangulation Estimation for Optical Window Free-Form Surfaces Testing by Coordinate Measuring Machine[J]. Photonics, 2025, 12(5): 469.

[25] Yu S, Yao P, Xu J, et al. Profile error compensation in ultra-precision grinding of aspherical-cylindrical lens array based on the real-time profile of wheel and normal residual error[J]. Journal of Materials Processing Technology, 2023, 312: 117849.

[26] Xu L, Fan F, Zhang Z, et al. Fast on-machine profile characterization for grinding wheels and error compensation of wheel dressing[J]. Precision Engineering-Journal of the International Societies for Precision Engineering and Nanotechnology, 2019, 55: 417-425.

[27] Grady D. Impact failure and fragmentation properties of tungsten carbide[J]. International Journal of Impact Engineering, 1999, 23(1):307-317.

[28] Grady D. Shock-wave compression of brittle solids[J]. Mechanics of Materials, 1998, 29(3-4):181-203.

[29] Shi L, Huang Y, Gao Y, et al. JH2 Constitutive Model of Inorganic Bulletproof Glass with Damage[J]. Chinese Journal of High Pressure Physics, 2024, 38(4): 044105.

[30] Zhu C, Sun Y, Wang D, et al. Evaluation and prediction of wrapping deformation in sheet part grinding[J]. Experimental Techniques, 2025,49(1):117-135.

[31] Chen G, Hu Z, Wang L, et al. Modeling of Material Removal Rate for the Fixed-Abrasive Double-Sided Planetary Grinding of a Sapphire Substrate[J]. Materials, 2024, 17(15): 3688.

Statements and Declarations

Funding

This work was supported by the National Natural Science Foundation of China (Grant No. 52305489), and the State Key Laboratory of Mechanical System and Vibration (Grant No. MSV202510).

Declaration of competing interest

The authors declare that they have no known competing financial interests or personal relationships that could have appeared to influence the work reported in this paper.

Data availability statement

Data will be made available on request.

Author Contributions

Peng Gu contributed to conceptualization, data curation, formal analysis, funding acquisition, and methodology. Kaixuan Zhou contributed to validation, visualization, and writing the original draft. Zhiyuan Li provided resources. Andrea Mura contributed to writing, review, and editing. Rumeng Yang contributed to formal analysis. Pengfei Zhang contributed to writing,

reviewing, and editing. Yingchen Sun contributed to software and validation. Chuanmin Zhu was responsible for project administration and supervision. All authors read and approved the final manuscript.